



1 A 25 km Daily Gridded Dataset of Meteorological Variables and High-Impact
2 Weather Events for New-type Power Systems in China (1980-2016)

3

4 Feimin Zhang¹, Kaixuan Bi¹, Xing Chen², Yi Yang¹, Fang Yang², Chenghai Wang¹

5 1. *Key Laboratory of Climate Resource Development and Disaster Prevention of*

6 *Gansu Province, Research and Development Center of Earth System Model (RDCM),*

7 *College of Atmospheric Sciences, Lanzhou University, Lanzhou, 730000, China.*

8 2. *Global Energy Interconnection Group Co., Ltd., Beijing, 100032, China.*

9

10

11

12

13

14

15

16

17 -----

18 *Corresponding Author Address: Dr. Feimin Zhang, College of Atmospheric Sciences,*

19 *Lanzhou University, Lanzhou, 730000, China*

20 E-mail: zfm@lzu.edu.cn

21



22 **Abstract:** The new-type power system exhibits pronounced “weather dependency”,
23 wherein high-impact weather events can significantly exacerbate operational security
24 risks. A high-quality gridded dataset that involves both meteorological variables and
25 high-impact weather events is of great significance for new-type power systems. In this
26 study, a spatially adaptive optimal interpolation scheme is developed and applied to
27 generate the China New-type Power Systems Meteorological (CNPS-Met) dataset. The
28 CNPS-Met dataset spans from 1980 to 2016 and covers the entire Chinese mainland,
29 with a daily temporal resolution and a 25 km spatial resolution. It includes eight
30 meteorological variables and eleven high-impact weather events, categorized from
31 generation-side, grid-side and demand-side perspectives relevant to new-type power
32 systems. Validation with existing datasets indicates that the CNPS-Met dataset
33 generally exhibits superior performance in meteorological estimation. Specifically, the
34 estimated mean relative errors for 2-m air temperature, 2-m specific humidity, 10-m
35 wind speed, precipitation and surface pressure averaged over the Chinese mainland
36 could be reduced by 1.7%-18.5%, 9.0%-29.6%, 1.9%-8.5%, 2.7%-18% and 4.9%-5.2%,
37 respectively. On this basis, a series of high-impact weather events critical to the
38 operation of new-type power system are identified. The spatial distribution of their
39 frequency hotspots and intensity extremes are further analyzed. The CNPS-Met dataset
40 is expected to benefit research and applications at the intersection of meteorology and
41 new-type power systems.
42



43 **1. Introduction**

44 A high-quality meteorological reanalysis dataset is of great significance for
45 analyzing climate change, verifying climate simulations, identifying high-impact
46 weather events, and predicting future climate change etc. (Qin et al. 2022; Wen et al.
47 2023). Over the past decades, China has built a large-scale ground-based
48 meteorological observation network, with the total number of ground-based
49 observations exceed 2400 (Xu et al. 2019). However, in regions with complex terrain
50 such as mountainous areas, the Tibetan Plateau, and the Gobi Desert, ground-based
51 observations are relatively sparse. As a result, the climate variability at small
52 geographic scales cannot be adequately represented (Wen et al. 2023; Jiang et al. 2023),
53 which constrains the practical applications of ground-based observations. Recently,
54 China has been building a new-type power system, with the core objective being to
55 maximize the integration of renewable energy such as wind and solar energy (Chapter
56 1 in Xin 2023). However, renewable energy integration is highly susceptible to weather
57 and climate (D'Amico et al. 2024; Gao et al. 2025). Against the backdrop of global
58 warming and increasing frequency of extreme weather events (IPCC AR6), significant
59 challenges are expected for the development of the new-type power system. Therefore,
60 to support both research and practical needs related to new-type power systems, it is
61 essential and urgent to develop a high quality gridded dataset that includes
62 meteorological variables and power system-relevant high-impact weather events.

63 Apart from several global atmospheric reanalysis datasets such as the ECMWF
64 (European Centre for Medium-Range Weather Forecasts) Reanalysis v5 (ERA5)



65 (Hersbach et al. 2020), and Modern-Era Retrospective analysis for Research and
66 Applications (MERRA) (Christensen et al. 2019) etc., several other widely used
67 gridded meteorological datasets covering China have recently been developed, most of
68 which are available at a daily scale. For instance, the gridded daily observation dataset
69 over China region (CN05.1) was developed based on approximately 2400 ground-based
70 observations in China. It has at spatial resolution of $0.25^{\circ} \times 0.25^{\circ}$ and covers the period
71 from 1961 to 2020, This dataset was constructed using spatial interpolation methods
72 (Wu and Gao 2013; Wu et al. 2017). The China Meteorological Forcing Data (CMFD)
73 dataset, spanning from 1951 to 2020 with a temporal resolution of 3 h and a spatial
74 resolution of $0.1^{\circ} \times 0.1^{\circ}$, was produced by integrating remote sensing products, ERA5
75 reanalysis, and approximately 400 ground-based observations in China. The
76 methodology employed interpolation techniques based on the ANUSPLIN software and
77 deep learning (He et al. 2020). More recently, the China Daily Meteorological Dataset
78 (CDMet), covering 2000 to 2020 at a spatial resolution of $4 \text{ km} \times 4 \text{ km}$, was generated
79 by merging ERA5 reanalysis with 699 ground-based observations across China. An
80 adaptive interpolation scheme combining thin-plate spline interpolation and random
81 forest algorithm was used in its production (Zhang et al. 2024). These datasets provide
82 useful basis for climate analysis, land surface and hydrology process study etc. (e.g.,
83 Qiu et al. 2024; Sutanto et al. 2024). Extreme weather and climate events can also be
84 derived from these datasets, using indices released by the World Meteorological
85 Organization (Heim et al. 2015). However, the definition of extreme weather and
86 climate events in atmospheric sciences, typically conceptualized as low-probability



87 events under large-sample assumptions, may not fully align with the operational needs
88 of new-type power systems. In fact, there are currently no dedicated datasets of extreme
89 or high-impact weather event categorized according to the generation-side, grid-side,
90 and demand-side needs of new-type power systems. Furthermore, although both the
91 CDMet and CMFD datasets incorporate diverse data sources, including satellite remote
92 sensing and reanalysis products, their utilization of ground-based observations remains
93 relatively limited. Over the complex terrain, ground-based observations have been
94 shown to possess superior accuracy and representativeness compared to satellite-
95 derived and reanalysis data (Wei et al. 2023; Rao et al. 2024; Jiang et al. 2025).

96 Another issue that requires attention is that the methodology employed in the
97 aforementioned datasets is fundamentally based on spatial interpolation. When limited
98 ground-based observations are used to generate gridded dataset at finer resolution, the
99 process effectively becomes extrapolation, meaning that estimates are made beyond the
100 boundaries of the original data coverage. In contrast, data assimilation, a well-
101 established technique in atmospheric modelling, aims to optimally combine
102 observations with background model fields to produce a more accurate estimate of the
103 true atmospheric state, while explicitly accounting for uncertainties in both the
104 observations and the model (Talagrand 1997). Additionally, data assimilation
105 incorporates information about the influence of climate condition on the spatial
106 distribution and relationships among meteorological variables (Kalnay 2003). In
107 practice, it has been widely used in operational numerical weather prediction and the
108 construction of gridded datasets (e.g., Kalnay 2003; Hunt et al., 2007; Bannister 2008;



109 Lee et al. 2013; Carrassi et al. 2018; Lindskog et al. 2019; Zhao et al. 2024). The optimal
110 interpolation (OI) is a classical data assimilation scheme known for its high
111 computational efficiency and reliable accuracy. It has been shown to be fundamentally
112 equivalent to more advanced methods such as the three-dimensional variational
113 assimilation (Gandin 1959; Akmaev 1999; Eyre et al. 2022). A key factor influencing
114 the performance of OI is the design of the observation operator (e.g., Daley 1993;
115 Uboldi et al. 2008; Girotto et al. 2020).

116 The Cressman interpolation method (Cressman 1959), which establishes the
117 relationship between observations and background field through a weight function, is
118 commonly used as observation operator in OI (Liu et al. 2016). However, in the
119 traditional Cressman interpolation, the influence radius in the weight function is
120 assumed to be a fixed constant. This assumption is reasonable in idealized situations
121 where observations are uniformly distributed, In cases of uneven observational
122 coverage, however, the use of a fixed radius can introduce significant errors and
123 uncertainties into the observation operator, thereby degrading the performance of the
124 OI scheme (e.g., Alonso et al. 2018; Miatselskaya et al. 2022; Wang et al. 2023; Jiang
125 et al. 2025). Therefore, dynamically adjusting the influence radius based on the spatial
126 distribution and density of observations around each grid point in the background field
127 would be a potential approach to improving observation operator and enhancing the
128 overall performance of OI.

129 The motivation of this study is to develop an improved OI assimilation scheme,
130 and to generate the China New-type Power Systems Meteorological (CNPS-Met)



131 dataset. This dataset includes eight meteorological variables and eleven high-impact
132 weather events, categorized according to three critical vulnerability dimensions:
133 generation-side, grid-side, and demand-side. A detailed description of the dataset is
134 provided in Table 1.

135 Table 1. Introduction to the CNPS-Met dataset.

Entry	Descriptions
Spatial coverage	The Chinese Mainland (excluding maritime territorial)
Temporal range	1980~2016
Spatial resolution	25 km×25 km
Temporal resolution	Daily
Time Standard	Universal Time Coordinated (UTC)
Format	NetCDF
Invalid value	-999.0
Abbreviation and introduction of meteorological variables	tas: 2-m mean temperature; tmax: 2-m maximum temperature; tmin: 2-m minimum temperature; precip: accumulated precipitation; wind: 10-m mean wind speed; rhum: 2-m mean relative humidity; shum: 2-m mean specific humidity; pres: mean surface pressure
Abbreviation for high-impact weather events in three critical vulnerability dimensions	Generation-side: Vout, Vin, Lowrad, Tmaxg, Tming Grid-side: Icing, Snowing, Galloping Demand-side: Tmaxd, Tmind, HHE

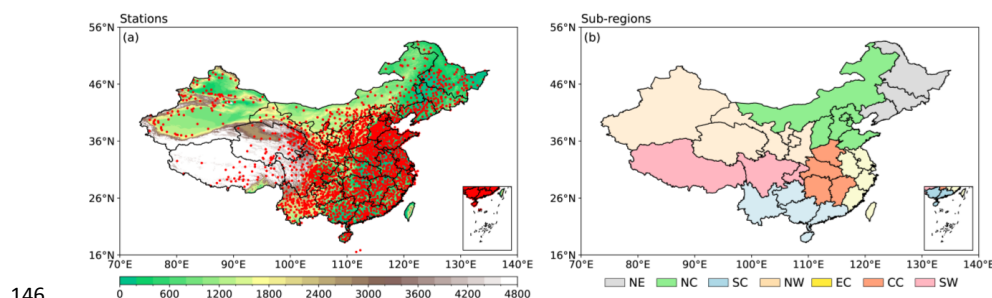
136 2. Data and methods

137 a. Modelling data

138 The CNPS-Met dataset is generated by fusing ground-based observations with
139 ERA5 reanalysis. The data from 2598 meteorological stations across China (Figure 1a),
140 spanning the period from 1980 to 2016, are used. These data include wind speed at 10
141 m, air temperature and relative humidity at 2 m, and surface pressure and precipitation,
142 and can be obtained from China Meteorological Administration (<https://data.cma.cn/>).
143 Prior to publication, the observations underwent strict quality control. The



144 meteorological stations are densely distributed in eastern and southern China but are
145 sparse in the northwestern regions and the Tibetan Plateau (Fig. 1a).



146
147 Figure 1. Distribution of (a) ground-based meteorological stations (red dots) and terrain height
148 (shaded colors), and (b) the seven sub-regions across Chinese mainland. The seven sub-regions
149 include Northeast China (NE), North China (NC), South China (SC), Northwest China (NW), East
150 China (EC), Central China (CC), and Southwest China (SW).

151 ERA5, the fifth generation of reanalysis data released by the ECMWF
152 (<https://cds.climate.copernicus.eu/datasets/reanalysis-era5-land?tab=overview>),
153 exhibits robust performance in China (Hersbach et al. 2020; Jiang et al. 2021; Lavers
154 et al. 2022). In this study, precipitation, surface pressure, wind speed at 10 m, air
155 temperature and specific humidity at 2 m, at horizontal resolution of $1^\circ \times 1^\circ$, are used
156 as background field in the assimilation. Specific humidity and relative humidity can be
157 mutually converted through thermodynamic formulas that incorporate air temperature
158 and pressure (Lovell-Smith et al. 2005).

159 To improve the accuracy of the input data and ensure the integrity of the CNPS-
160 Met dataset, we exclude the anomalous records by detecting records that are deviated
161 significantly from their mean values using the three-sigma rule method (Oakland and
162 Oakland 2007).



163 *b. Validation data*

164 The daily CN05.1, CMFD and CDMet gridded datasets are used to validate the
165 CNPS-Met dataset. Although the CMFD has the sub-daily (3-hourly) records, it is
166 primarily derived from the ERA5 reanalysis and remote sensing products, rather than
167 ground-based observations. Therefore, daily datasets are validated in this study. In
168 addition, although the CMFD and CDMet have horizontal resolutions of 10 km and 4
169 km, respectively, they are generated essentially by spatial interpolation rather than
170 fusing additional observations. Hence, all datasets are interpolated to a common
171 horizontal resolution of $0.25^\circ \times 0.25^\circ$.

172 *c. Spatially adaptive optimal interpolation assimilation scheme*

173 The Optimal Interpolation (OI) assimilation scheme is employed to generate the
174 CNPS-Met dataset. This scheme estimates optimal values by minimizing the errors
175 between the observations and the background fields. The objective function is defined
176 as follows:

177
$$\mathbf{x}_a = \mathbf{x}_b + \mathbf{W}[\mathbf{y}_o - \mathbf{H}(\mathbf{x}_b)] \quad (1)$$

178 where \mathbf{x}_a is the analysis field (optimal field), \mathbf{x}_b is the background field (e.g.,
179 ERA5 reanalysis), they are both the matrix of $m \times n$ (grid points in the latitudinal and
180 meridional directions, respectively); \mathbf{y}_o is the observations, which is the vector with a
181 length of p (e.g., number of ground-based stations); the two-dimensional matrix \mathbf{H} is
182 the observation operator, which maps values from regularly gridded background fields
183 to irregularly distributed ground-based station observations; \mathbf{W} is the optimal weight
184 matrix, which can be written as:



$$185 \quad \mathbf{W} = \mathbf{B}\mathbf{H}^T (\mathbf{H}\mathbf{B}\mathbf{H}^T + \mathbf{R})^{-1} \quad (2)$$

186 where superscript T denotes the matrix transpose operation; \mathbf{B} is the background
 187 error covariance matrix, and \mathbf{R} is the observation error covariance matrix, they can be
 188 written as:

$$189 \quad \mathbf{B} = \mathbf{E} \{ \boldsymbol{\varepsilon}_b \boldsymbol{\varepsilon}_b^T \} \quad (3)$$

$$190 \quad \mathbf{R} = \mathbf{E} \{ \boldsymbol{\varepsilon}_o \boldsymbol{\varepsilon}_o^T \} \quad (4)$$

191 where $\boldsymbol{\varepsilon}_b$ is the vector of grid points variances and covariances in the background
 192 filed over a given period (e.g., one month), while $\boldsymbol{\varepsilon}_o$ is the corresponding vector of
 193 variances and covariances for ground-based station observations over the same period;
 194 \mathbf{E} represents a two-dimensional matrix. From the above equations, it is clear that given
 195 the observations (\mathbf{y}_o) and the background field (\mathbf{x}_b), the background error covariance
 196 matrix (\mathbf{B}) and the observation error covariance matrix (\mathbf{R}) are determined.
 197 Consequently, the performance of the OI assimilation scheme depends solely on the
 198 observation operator (\mathbf{H}).

199 The observation operator (\mathbf{H}), implemented here using Cressman interpolation,
 200 applies a distance-dependent weighting function to compute a weighted average of
 201 observations, with weights monotonically decreasing as a function of distance, thereby
 202 emphasizing the contribution of local observations to the final interpolated field. The
 203 observation operator can be determined via iterative updating as follows:

$$204 \quad \mathbf{H}^y = \frac{\sum_{k=1}^K (w_{ijk}^2 \Delta \alpha_k^y)}{\sum_{k=1}^K w_{ijk}} \quad (5)$$

205 where $\Delta \alpha_k^y = \mathbf{y}_o(k) - \mathbf{x}_b^y$ denotes the difference between observation at k^{th}



206 ground-based station and grid point (i, j) at γ^{th} iteration; K denotes the number of total
207 ground-based stations ; $\mathbf{x}_b^Y = \mathbf{x}_b^{Y-1} + \mathbf{H}^{Y-1}$ denotes updated temporary background
208 filed at γ^{th} iteration, which will be used to continuously update $\Delta\alpha_k^Y$ and \mathbf{H}^Y , the
209 ERA5 reanalysis will be used as first guess in the iteration; the iteration termination
210 condition is $|\Delta\alpha_k^Y| \leq 1 \times 10^{-6}$, the resulting \mathbf{H}^Y will be then used as the definitive
211 observation operator (\mathbf{H}) in Eqs. (1-2) to perform OI assimilation; w_{ijk} is the weight
212 function in Cressman interpolation, its expression can be written as:

$$213 \quad w_{ijk} = \begin{cases} \frac{R_c(i, j)^2 - d_{ijk}^2}{R_c(i, j)^2 + d_{ijk}^2}, & d_{ijk} \leq R_c(i, j) \\ 0, & d_{ijk} > R_c(i, j) \end{cases} \quad (6)$$

214 where d_{ijk} represents the spatial distance between grid point (i, j) and
215 observation at k^{th} ground-based station; $R_c(i, j)$ represents the influence radius.

216 In the traditional Cressman interpolation, the influence radius is typically held
217 constant. While this assumption is reasonable in regions with uniformly distributed
218 observation stations, it would become problematic in practice due to the inherently
219 uneven distribution of stations, especially over complex terrain. Such non-uniformity
220 can degrade the performance of Cressman interpolation (Lin et al. 2012; Wang et al.
221 2023), and consequently impair the accuracy of OI assimilation scheme. To overcome
222 this limitation, this study introduces a spatially adaptive influence radius that adjusts
223 according to local observation density and distribution. This enhancement would
224 improve the observation operator and optimizes the overall OI assimilation framework.
225 The proposed method is referred to as the spatially adaptive OI assimilation scheme.
226 The spatially varying influence radius $R_c(i, j)$ is calculated as follows:



$$R_c(i, j) = \min \left\{ R \mid \hat{K}(i, j, R) \geq N_{min}, R_{min} \leq R \leq R_{max} \right\} \quad (7)$$

where $\hat{K}(i, j, R)$ denotes the number of observation stations within a circle of search radius R centered at grid point (i, j) ; the lower limit R_{min} is 1 km, while the upper limit R_{max} is set to 200 km; N_{min} represents the preset minimum threshold for the number of observation stations within the search radius R . As expressed in Eq. (7), the influence radius $R_c(i, j)$ at grid point (i, j) is determined as the smallest search radius R for which the number of surrounding observation stations $\hat{K}(i, j, R)$ satisfies $\hat{K}(i, j, R) \geq N_{min}$, obtained through a loop search process. The preset threshold N_{min} can be continuously refined through verification of the analysis field (\mathbf{x}_a) against observations.

d. Statistics for verification

The performance of the CNPS-Met dataset is evaluated using the statistics including the mean relative error (*MRE*), the root mean square error (*RMSE*), correlation coefficient (R^2), and the modeling efficiency (*EF*):

$$MRE = \frac{1}{n} \sum_{i=1}^n |(P_i - O_i) / O_i| \quad (8)$$

$$RMSE = \sqrt{\frac{1}{n} \sum_{i=1}^n (P_i - O_i)^2} \quad (9)$$

$$R^2 = \frac{\left[\sum_{i=1}^n (O_i - \bar{O})(P_i - \bar{P}) \right]^2}{\sum_{i=1}^n (O_i - \bar{O})^2 \sum_{i=1}^n (P_i - \bar{P})^2} \quad (10)$$

$$EF = 1 - \frac{\sum_{i=1}^n (P_i - O_i)^2}{\sum_{i=1}^n (O_i - \bar{O})^2} \quad (11)$$

where n denotes sample size; O_i and P_i are the observed and estimated values,



246 respectively; \bar{O} and \bar{P} are the average of the observed and estimated values,
247 respectively. The *MRE* and *RMSE* closer to 0, and the R^2 and *EF* closer to 1
248 indicate better estimation performance.

249 Apart from the above statistics, a more comprehensive statistic referred as the
250 global performance index (*GPI*; Despotovic et al. 2015), is introduced in this study:

$$251 \quad GPI = \sum_{k=1}^4 \alpha_k (\bar{y}_k - y_k) \quad (12)$$

252 where \bar{y}_k represents the median of the scaled values of indicator k (i.e., *MRE*,
253 *RMSE*, R^2 and *EF*); y_k is scaled value of indicator k ; $\alpha_k = 1$ corresponds to
254 *MRE* and *RMSE*, while $\alpha_k = -1$ corresponds to R^2 and *EF*. The higher the *GPI*,
255 the better performance of the overall estimation.

256 *e. Identification of high-impact weather events for new-type power systems*

257 Based on a comprehensive review of the existing literatures, the high-impact
258 weather events for the generation-side, grid-side and demand-side of new-type power
259 systems could be defined in Table 2. In the generation-side, cut-out wind speed is
260 defined as hourly wind speed reaches or exceeds 25 m s^{-1} , that is, wind turbine
261 automatically shuts down to prevent equipment damage when wind speeds reach or
262 exceed this threshold, resulting in an abrupt reduction of wind power output to zero
263 (Jerez et al. 2015; Song et al. 2022). According to Jerez et al. (2015) and Song et al.
264 (2022), cut-in wind speed is defined as hourly mean wind speeds $\leq 2.5 \text{ m s}^{-1}$, that is,
265 wind turbines would remain in standby or idle mode when wind speed is less than or
266 equal to this threshold, resulting in effectively zero power output. Based on the
267 observations of hourly solar irradiance and power generation efficiency in large-scale



268 photovoltaic power plants, Sundaram et al. (2024) demonstrated that photovoltaic
 269 conversion efficiency decreases significantly when hourly solar irradiance falls below
 270 100 W m^{-2} , with the performance ratio declining to critical levels; supporting this
 271 finding, Lei et al. (2025) established through comprehensive literature reviews that
 272 $\leq 100 \text{ W m}^{-2}$ represents the standardized threshold for low-light conditions in
 273 photovoltaic systems; therefore, low radiation is defined as hourly solar irradiance
 274 $\leq 100 \text{ W m}^{-2}$. Through systematic analysis of measurements and experiments (Oloufemi
 275 et al. 2016; Mohammad et al. 2021; Yang et al. 2022; Sun et al. 2022; Ju et al. 2022;
 276 Köster et al. 2023), Bi et al. (2025) derived a fitted relationship between power
 277 generation loss and air temperature; for operational definitions, extreme high
 278 temperature is specified as $\geq 35 \text{ }^\circ\text{C}$, while extreme low temperature is defined as \leq -
 279 $20 \text{ }^\circ\text{C}$.

280 Table 2. Classification and definition of high-impact weather events for new-type power systems.

Components of new-type power system	High-impact weather events	Abbreviation	Definition	Impacts on new-type power systems	References
Generation-side	Cut-out wind speed	Vout	Hourly wind speed $\geq 25 \text{ m s}^{-1}$	Wind turbine shutdown causes abrupt drop in wind power output to zero	Song et al. (2022) Jerez et al. (2015)
	Cut-in wind speed	Vin	Hourly wind speed $\leq 2.5 \text{ m s}^{-1}$	Wind turbine remains in standby or idle mode, resulting in abnormal zero power output	Song et al. (2022) Jerez et al. (2015)
	Low	Lowrad	Hourly	Reduces the	Sundaram



	radiation		radiation $\leq 100 \text{ W m}^{-2}$	efficiency of photovoltaic conversion	et al. (2024) Lei et al. (2024)
	Extreme high temperature	Tmaxg	Hourly temperature $\geq 35 \text{ }^\circ\text{C}$	Overloading of power equipment leads to loss of power generation efficiency	Mohammad et al. (2021) Yang et al. (2022)
	Extreme low temperature	Tming	Hourly temperature $\leq -20 \text{ }^\circ\text{C}$	Equipment shutdown resulting in loss of power generation efficiency	Ju et al. (2022) Sun et al. (2022)
	Ice accretion	Icing	Hourly temperature $\leq 0 \text{ }^\circ\text{C}$, hourly relative humidity $\geq 85\%$, and hourly wind speed $\leq 4 \text{ m s}^{-1}$ simultaneously	Significantly increases the mechanical load on transmission lines, causing line breakage, flashover, and tripping	Gu et al. (2010) Shen et al. (2010) Pei et al. (2024)
Grid-side	Snowfall	Snowing	Hourly precipitation $\geq 0.1 \text{ mm}$ and hourly temperature $\leq 0 \text{ }^\circ\text{C}$ simultaneously	Increases the risk of line icing, damages the structural strength of power facilities, and threatens the reliability of power supply	Iver et al. (2019) Wesley et al. (2020)
	Conductor galloping	Galloping	Hourly relative humidity $\geq 75\%$ and wind speeds exceeding 4 m s^{-1} persisted for more than 3 hours simultaneously	Cause short circuit tripping of the line and may lead to chain faults	Tsujimoto et al. (1983) Li et al. (2015)
Demand-side	Extreme high	Tmaxd	Hourly temperature ≥ 38	The demand for electricity load	Fu et al. (2015)



temperature		°C	would sharply increase	Ye et al. (2024)
Extreme low temperature	Tmind	Hourly temperature ≤ -10 °C	The sensitivity of electricity load demand would sharply increase to extreme low temperature	Blake et al. (2022) Millin et al. (2024)
Heat and humid environment (High enthalpy environment)	HHE	Hourly temperature ≥ 28 °C and relative humidity $\geq 65\%$ simultaneously	Significantly increases the risk of human heat stress and exacerbates the load on power equipment	Patrick et al. (2015) Jane et al. (2023)

281 In the grid-side, ice accretion is defined as hourly air temperature ≤ 0 °C, hourly
 282 relative humidity $\geq 85\%$ and hourly wind speed ≤ 4 m s⁻¹; this definition is supported
 283 by three evidences: first, thermodynamic analysis by Gu et al. (2010) demonstrated
 284 through thermal equilibrium theory and wind tunnel experiments that the required Joule
 285 heating for anti-icing systems exhibits a sharp decline when temperatures fall below
 286 0 °C, indicating a fundamental threshold for ice formation; second, comprehensive field
 287 observations by Shen et al. (2010) established the multi-parameter requirements for ice
 288 accretion on transmission lines, that are, the critical thermal window (temperature ≤ 0
 289 °C, with optimal range between -10 °C and -1 °C), the moisture threshold (relative
 290 humidity $\geq 85\%$ for sufficient water vapor supply), and the aerodynamic constraint
 291 (wind speed ≤ 4 m s⁻¹ to enable effective droplet impingement while preventing wind-
 292 driven shedding); third, these parameters are also codified in the Chinese
 293 Meteorological Industry Standard QX/T 355-2016 for wire icing risk assessment, which
 294 formally defines ice accretion as “the adherence of glaze, rime, or frozen wet snow to



295 conductors” (Pei et al. 2024). Tsujimoto et al. (1983) found that conductor galloping
296 typically occurs when wind speeds $\geq 4 \text{ m s}^{-1}$ and persist for over 3 hours; Li et al. (2015)
297 further established meteorological thresholds by analyzing hourly weather variations
298 during galloping events and considering galloping mechanisms and grid operation
299 experience; based on these studies, the galloping criterion in this study is defined as:
300 hourly relative humidity $\geq 75\%$ with sustained ($\geq 3 \text{ h}$) wind speeds $\geq 4 \text{ m s}^{-1}$. Snowfall
301 is defined as hourly precipitation $\geq 0.1 \text{ mm}$ with air temperature $\leq 0 \text{ }^\circ\text{C}$, consistent
302 with the standard definition adopted in community land surface models (Oleson et al.
303 2013).

304 In the demand-side, Fu et al. (2015) investigated the response of observed daily
305 peak power load to temperature variations, identifying $38 \text{ }^\circ\text{C}$ as a critical threshold for
306 peak power load, beyond which demand surges dramatically; observation analysis of
307 Shaffer et al. (2022) found that power demand sensitivity increases sharply below -10
308 $^\circ\text{C}$; similarly, Millin et al. (2024) observed significant load anomalies below $-6 \text{ }^\circ\text{C}$ in
309 the U.S. Midwest; accordingly, we define extreme high and low temperature thresholds
310 as: hourly temperature $\geq 38 \text{ }^\circ\text{C}$ and $\leq -10 \text{ }^\circ\text{C}$, respectively. Baldwin et al. (2023)
311 demonstrated through physiological experiments and observations that combined
312 thermal stress (air temperature $\geq 30 \text{ }^\circ\text{C}$ with relative humidity $\geq 65\%$) significantly
313 increases human heat strain risks in power load sectors; Sullivan et al. (2015) further
314 identified $28 \text{ }^\circ\text{C}$ as the critical temperature threshold for notable load growth through
315 hourly load-temperature analysis; accordingly, heat and humid environment (high
316 enthalpy environment) is defined as: hourly temperature $\geq 28 \text{ }^\circ\text{C}$ with relative



317 humidity $\geq 65\%$.

318 We need to explain that although these high-impact weather events are defined
319 through literature reviews, their definitions are grounded in empirical evidence derived
320 from observational studies, controlled laboratory experiments, or synthesis of
321 established research findings. Therefore, the resulting classifications should be both
322 scientifically reasonable and reliable. For high-impact weather events such as ice
323 accretion, conductor galloping, and heat and humid environment in Table 2, as they
324 involve multiple meteorological variables, the following composite weather index
325 (*CWI*) is defined to characterize their occurrence and intensity:

$$326 \quad CWI = \begin{cases} \prod_{k=1}^n \frac{\alpha_k - th(\alpha_k)}{\max(\alpha_k) - th(\alpha_k)}, & \alpha_1 \geq th(\alpha_1), L, \alpha_k \geq th(\alpha_k) \\ 0 & , else \end{cases} \quad (13)$$

327 where α represents a high-impact weather event composed of n meteorological
328 variables, where the index of each variable is denoted by subscript k ($k=1, 2, \dots, n$).
329 The threshold and the daily maximum value of the k -th variable α_k are denoted as
330 $th(\alpha_k)$ and $\max(\alpha_k)$, respectively.

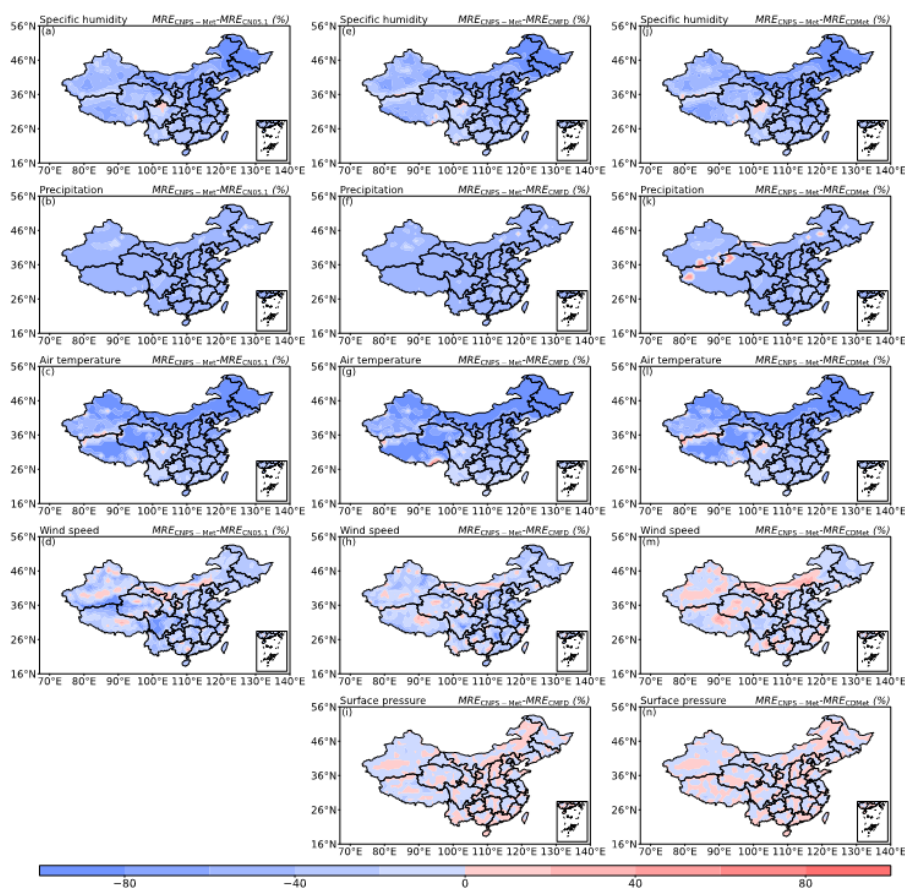
331 To analyze high-impact weather events affecting new-type power systems across
332 different regions of China, seven sub-regions are divided according to the spatial
333 distribution and organizational characteristics of the power grid in China (Fig. 1b).

334 3. Verification of the CNPS-Met dataset

335 Figure 2 shows the spatial distribution of differences in *MREs* of various
336 meteorological variables between the CNPS-Met dataset and three other widely used
337 datasets (CN05.1, CMFD and CDMet). Results show that the CNPS-Met dataset



338 achieves lower *MREs* across different meteorological variables and over the majority
339 region of China compared to the other datasets, indicating a generally higher accuracy
340 of the meteorological estimates in CNPS-Met. Significant improvements are
341 particularly evident in humidity, temperature and precipitation. However, exceptions
342 are observed in some regions along the periphery of the Tibetan Plateau, where
343 performance gains are less pronounced. Compared to the other datasets, the
344 improvement in wind speed within CNPS-Met remains limited. Consistent results can
345 also be found in different seasons (not shown). These discrepancies may be attributed
346 to the following factors. First, the OI assimilation scheme employed in this study relies
347 on background and observation error covariance matrices [Eqs. (3-4)] derived from
348 monthly-scale statistics. These matrices are static and may fail to adequately capture
349 the rapid temporal variation characteristics of highly transient and intermittent variables
350 such as wind speed. Second, regions where CNPS-Met exhibits larger errors are
351 characterized by complex terrain and sparse observational coverage, the inherent
352 uncertainties in the background field (e.g., ERA5) would diminish the effectiveness of
353 the assimilation performance in these regions.



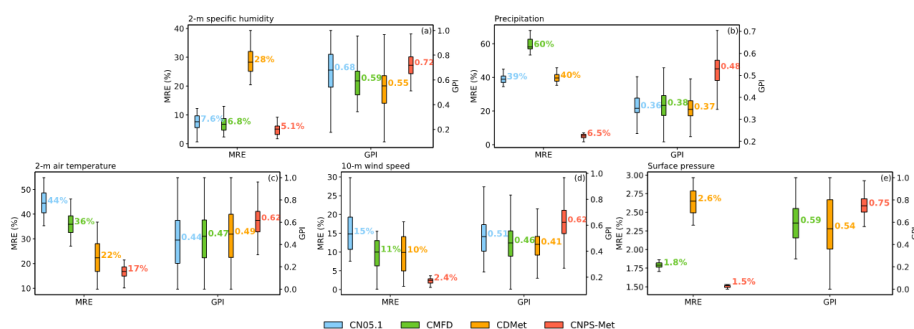
354

355 Figure 2. Spatial distribution of the differences in the mean $MREs$ (unit: %; averaged over 1980-
 356 2016) between three dataset pairs: (a-d) CNPS-Met and CN05.1 ($MRE_{CNPS-Met} minus MRE_{CN05.1}$),
 357 (e-i) between CNPS-Met and CMFD ($MRE_{CNPS-Met} minus MRE_{CMFD}$), and (j-n) between CNPS-Met
 358 and CDMet ($MRE_{CNPS-Met} minus MRE_{CDMet}$). The differences are shown for (a, e, j) 2-m specific
 359 humidity, (b, f, k) precipitation, (c, g, l) 2-m air temperature, (d, h, m) 10-m wind speed, and (i, n)
 360 surface pressure. Note that CN05.1 dataset does not include surface pressure.

361 Figure 3 displays box plots of the $MREs$ and GPI values across different datasets
 362 and meteorological variables, averaged over China for the period 1980-2016. In
 363 comparison to the other datasets, CNPS-Met exhibits the lowest $MREs$ with the



364 narrowest range. Similarly, the *GPI* values in CNPS-Met are generally closest to 1.0
365 and show the lower variability among the datasets. These results collectively indicate
366 that the CNPS-Met dataset achieves superior performance over existing alternatives.

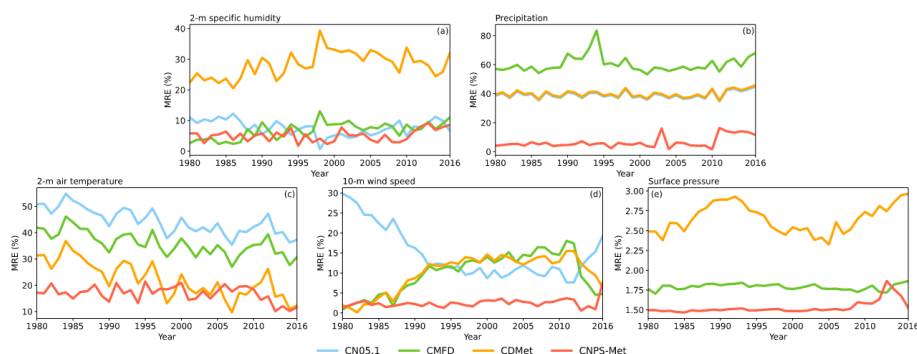


367
368 Figure 3. The mean *MREs* (unit: %) and *GPIs* (unit: dimensionless) averaged over China from 1980
369 to 2016 in different datasets for (a) 2-m specific humidity, (b) precipitation, (c) 2-m air temperature,
370 (d) 10-m wind speed, and (e) surface pressure.

371 To evaluate the effects of CNPS-Met at temporal scale, Figure 4 compares the
372 annual variations of *MREs* in China for different meteorological variables across
373 different datasets. Results show that CNPS-Met generally outperforms other datasets in
374 most years, especially for precipitation, wind speed and surface pressure. Exceptions
375 occur for air temperature and specific humidity, where *MREs* from CNPS-Met are larger,
376 such as near 1985 and between 2005 and 2010. The monthly *MREs* across different
377 datasets and meteorological variables, averaged over China for the period 1980-2016,
378 are further compared in Figure 5. Consistent with the above results, CNPS-Met
379 outperforms the other datasets in different months, exhibiting generally the lowest
380 *MREs* and narrowest variability range. As noted earlier, the improvement effect of
381 CNPS-Met on precipitation remains modest compared to that on other meteorological

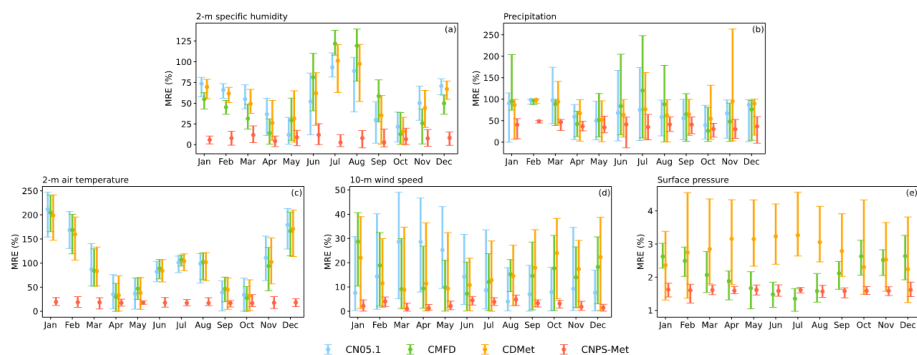


382 variables.



383

384 Figure 4. The inter-annual variation of the mean *MREs* (unit: %; averaged over China) for (a) 2-m
385 specific humidity, (b) precipitation, (c) 2-m air temperature, (d) 10-m wind speed and (e) surface
386 pressure in different datasets.



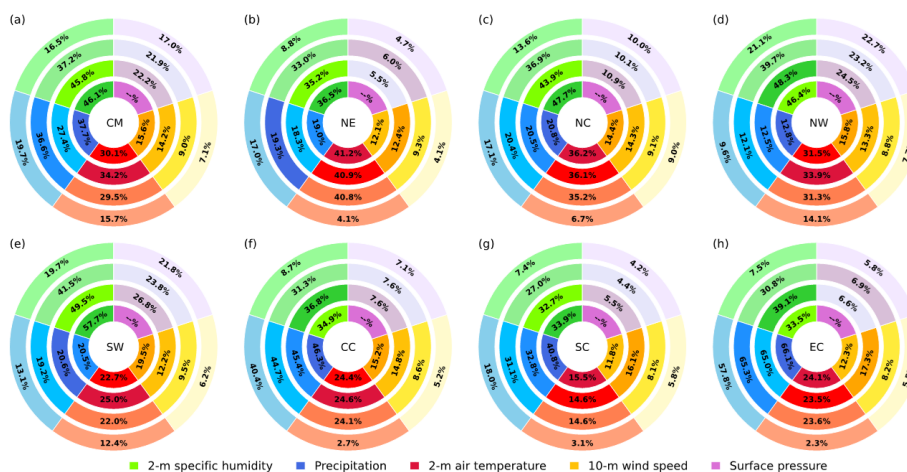
387

388 Figure 5. Monthly variation of the mean *MREs* (unit: %; averaged in China from 1980 to 2016) for
389 (a) 2-m specific humidity, (b) precipitation, (c) 2-m air temperature, (d) 10-m wind speed and (e)
390 surface pressure in different datasets.

391 Given the apparent spatial heterogeneity of *MREs* across different datasets (Fig.
392 2), Figure 6 presents the *MREs* averaged over the period from 1980 to 2016 for China
393 and its seven sub-regions. Results show that among all datasets evaluated, CNPS-Met
394 demonstrates the lowest *MREs* in various meteorological variables over both the entire



395 China region and its seven sub-regions. In addition to the findings consistent with the
396 analysis above, that are, the *MREs* for different meteorological variables in CNPS-Met
397 are the smallest. Compared to the other three datasets, *MREs* of air temperature, specific
398 humidity, wind speed, precipitation and surface pressure averaged over China for the
399 past 40 years could be reduced by 1.7%-18.5%, 9.0%-29.6%, 1.9%-8.5%, 2.7%-18%
400 and 4.9%-5.2%, respectively. For specific humidity, CNPS-Met exhibits relatively
401 small *MREs* (7-9%) in South China (SC), East China (EC), Central China (CC), and
402 Northeast China (NE), whereas relatively large *MREs* (approximately 20%) are
403 observed in Northwest China (NW) and Southwest China (SW). For wind speed, the
404 smallest *MRE* (4.1%) occurs in Northeast China (NE), while the largest *MRE* (9.0%) is
405 found in North China (NC). In the case of air temperature, smaller *MREs* (below 3%)
406 are exhibited in East China (EC) and Central China (CC), contrasting with the largest
407 *MREs* (14.1%) in Northwest China (NW). For precipitation, the smallest *MRE* (9.6%)
408 is observed in Northwest China (NW), compared to the largest *MRE* (57.8%) in East
409 China (EC). For surface pressure, the smaller *MRE* (below 10%) occurs in Northeast
410 China (NE), North China (NC), Central China (CC), South China (SC) and East China
411 (EC), while the larger *MRE* (9.0%) is found in other regions. Noted that the
412 improvement of CNPS-Met in wind speed is relatively modest compared to other
413 datasets (see Figs. 2). However, wind speed in CNPS-Met exhibits the smallest *MREs*
414 among all meteorological variables, similar phenomenon can also be observed in other
415 datasets (see Figs. 4-6).



416

417 Figure 6. The mean *MREs* (unit: %; averaged over 1980-2016) of different meteorological variables
 418 in (a) Chinese mainland (CM), (b) Northeast China, (c) North China, (d) Northwest China, (e)
 419 Southwest China, (f) Central China, (g) South China, and (h) East China. The concentric circles
 420 represent different datasets (from inner to outer: CN05.1, CMFD, CDMet and CNPS-Met. The
 421 lowest values of *MREs* are denoted as the lightest color. The mean *MREs* for surface pressure are
 422 denoted as --%, as it is not included in the CN05.1 dataset.

423 **4. Characteristics of high-impact weather events for new-type power systems**

424 In this section, high-impact weather events from three critical dimensions of the
 425 new-type power system such as generation-side, grid-side, and demand-side will be
 426 identified from Table 2, followed by a discussion of their spatiotemporal characteristics
 427 in the past 40 years.

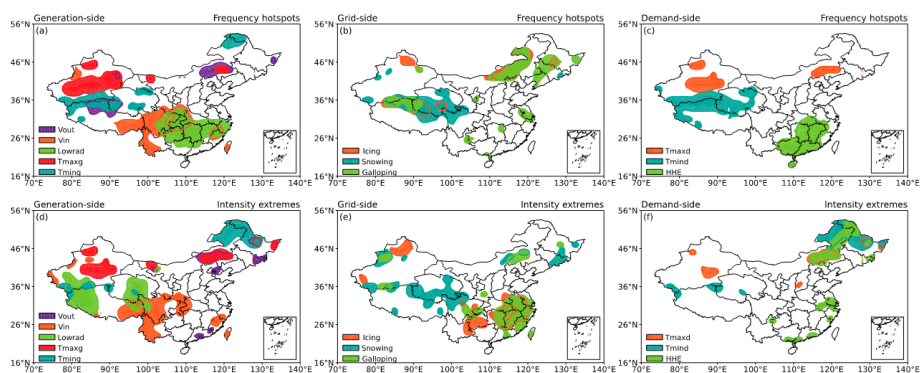
428 Figure 7 shows the spatial distribution of the multi-year averaged frequency
 429 hotspots and intensity extremes (90% confidence level) of different high-impact
 430 weather events in China. In the generation-side, cut-out wind speed predominantly
 431 occurs over the Northern Tibet Plateau, Eastern Inner Mongolia, and parts of Xinjiang



432 known as the “Hundred-mile Wind Zone”, which is consistent with the regions of high
433 wind energy potentials, as analyzed by Pan et al. (2012), Yao et al. (2018) and Gyatso
434 et al. (2023). Cut-in wind speed are primarily observed in Southwest China, this spatial
435 pattern aligns with existing research on sustained weak wind events in Chinese
436 Mainland, which are known to severely impact generation-side reliability (Gao et al.
437 2025). Low radiation events are concentrated in the middle and lower reaches of the
438 Yangtze River. This finding is consistent with Zhang et al. (2024), who attribute the
439 region’s lower solar radiation to its higher cloud cover and humidity. Extreme high
440 temperatures are primarily found in the desert regions of Xinjiang (i.e., Junggar and
441 Tarim basins), as well as in Eastern Inner Mongolia, a pattern highly consistent with
442 existing climate model simulation and observations and largely attributed to regional
443 arid conditions (Meng et al. 2019; Dong et al. 2024). Extreme low temperatures occur
444 most frequently in the Kunlun Mountains, the Qilian Mountains and Northeast China,
445 which is consistent with Yang et al. (2015) and Shi et al. (2016), who note that despite
446 a general decline trend of extreme low temperatures, these regions remain prone to such
447 events. In the grid-side, ice accretion primarily affects Northeast China, Northern
448 Xinjiang and Kunlun Mountains, which is also reported by Chen et al. (2010). Snowfall
449 events are most frequent across the Tibetan Plateau, Northeast China, and Northwest
450 Xinjiang, this distribution pattern is consistent with the findings of Yang et al. (2019)
451 and Wang et al. (2022) based on their analysis of observations and multi-source
452 reanalysis datasets. Conductor galloping occurs mainly in Northeast China, Northern
453 Tibetan Plateau, and sporadic regions in southern China. The spatial distributions of



454 extreme high- and low-temperature frequencies in the demand-side are similar to those
455 in the generation-side. Heat and humid environments occur primarily in Central and
456 Southern China, consistent with Li et al. (2025) regarding their impact on the demand-
457 side. The spatial distributions of high-impact weather intensity and frequency are
458 generally consistent, albeit with some exceptions. For example, in the generation-side,
459 low solar radiation events are most frequent in the middle and lower reaches of the
460 Yangtze River, yet they are relative weak when they occur. In the grid-side, ice accretion
461 is infrequent in Southern China but tends to be intense. In the demand-side, the extreme
462 low temperatures in Northeast China are particularly severe.

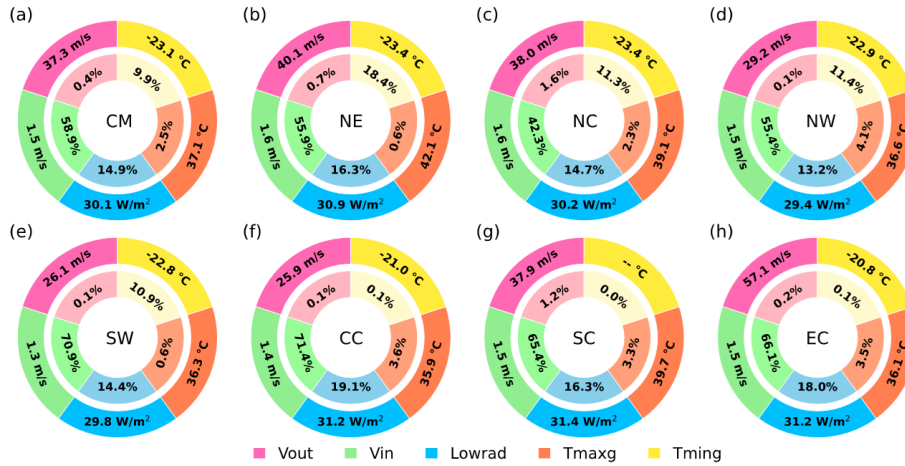


463
464 Figure 7. Spatial distribution of frequency hotspots and intensity extremes (90% confidence level)
465 of different high-impact weather events in Chinese mainland during 1980-2016.

466 Figures 8-10 summarize the frequency and intensity of high-impact weather events
467 in the generation-side, grid-side and demand-side in China and its sub-regions. In the
468 generation-side, the highest frequency of cut-out wind speed occurs in North China,
469 while its highest intensity is in East China. Cut-in wind speed is most frequent in
470 Southwest and Central China. Low radiation occurs most frequently in East and Central
471 China. Extreme high temperatures are relatively frequent in Northwest, Central, East

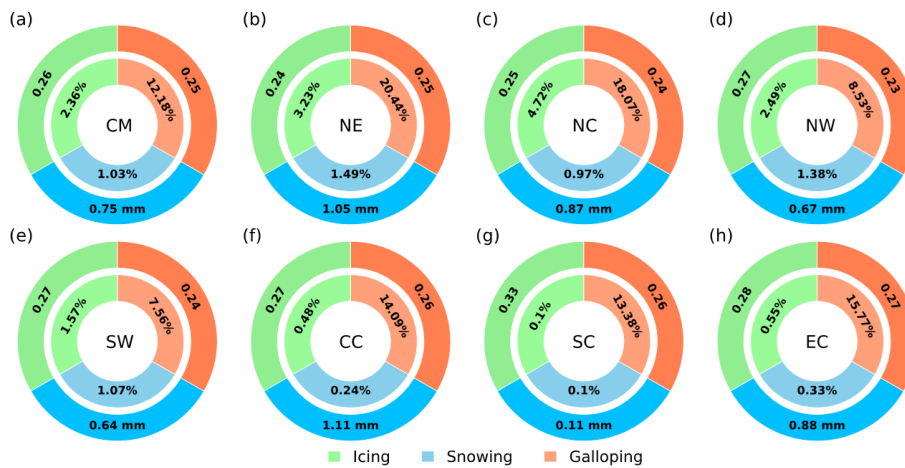


472 and South China, with the greatest intensity observed in North China. Extreme low
473 temperatures are most frequent and most intense in Northeast China. On average, the
474 frequency and mean intensity of cut-out wind speed, cut-in wind speed, low radiation,
475 extreme high temperature and extreme low temperature in China are 0.4% and 37.3 m
476 s^{-1} , 58.9% and 1.5 $m s^{-1}$, 14.9% and 30.1 $W m^{-2}$, 2.5% and 37.1 $^{\circ}C$, 9.9% and -23.1 $^{\circ}C$,
477 respectively. In the grid-side, ice accretion occurs most frequently in North China while
478 its most severe events are observed in South China. Snowfall events are most frequent
479 in Northeast China, while are most intense in Central China. Conductor galloping
480 events are most common in Northeast China while their peak intensity is found in East
481 China. On average, the frequency and mean intensity of ice accretion, snowfall and
482 conductor galloping events in China are 2.36% and 0.26, 1.03% and 0.75 mm, and
483 12.18% and 0.25, respectively. In the demand-side, both the frequency and intensity of
484 extreme high temperature are relatively high in Northwest and South China. Extreme
485 low temperature reach its highest frequency and intensity in Northeast China. Similarly,
486 heat and humid environment is most pronounced in South, East and Central China. On
487 average, the frequency and mean intensity of extreme high temperature, extreme low
488 temperature and heat and humid environment in China are 0.73% and 40.94 $^{\circ}C$, 24.84%
489 and -15.06 $^{\circ}C$, and 6.07% and 0.24, respectively.



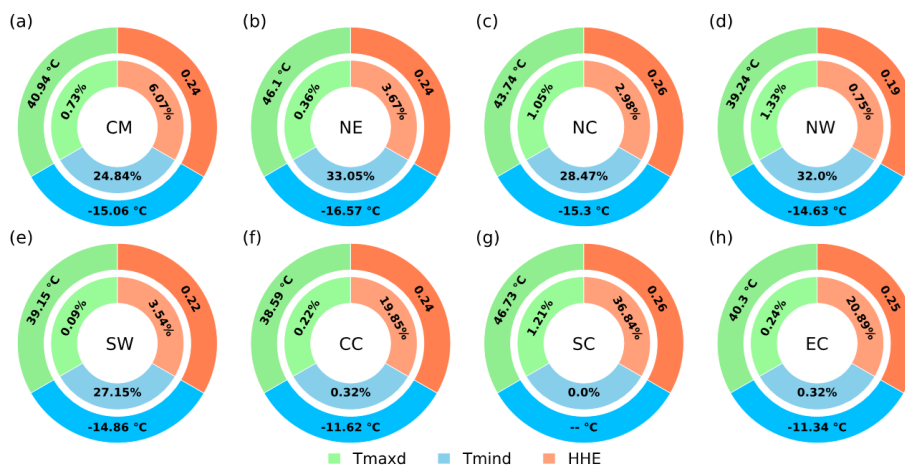
490

491 Figure 8. The annual mean frequency (unit: %/a) and intensity of high-impact weather events
 492 relevant to generation-side across different regions of China (1980 to 2016). The inner and outer
 493 circles correspond to the frequency and average intensity, respectively.



494

495 Figure 9. Similar to Fig. 8, but for grid-side. Note that the intensity of ice accretion and conductor
 496 galloping events is calculated based on *CWI* indice, which is dimensionless.



497

498 Figure 10. Similar to Fig. 8, but for demand-side. Note that the intensity of heat and humid
499 environment events is calculated based on *CWI* indice, which is dimensionless.

500 5. Concluding remarks

501 In new-type power systems dominated by wind and solar energy, there is a
502 pronounced “weather dependency” and “system vulnerability”, where high-impact
503 weather events can amplify risks to operational security. Developing a high-quality
504 gridded dataset that involves both meteorological variables and high-impact weather
505 events is of great significance. In this study, the China New-type Power Systems
506 Meteorological (CNPS-Met) dataset is developed, and the spatiotemporal
507 characteristics of high-impact weather events affecting new-type power systems are
508 analyzed. The main conclusions are summarized as follows:

509 An improved optimal interpolation assimilation scheme, herein referred to as the
510 spatially adaptive optimal interpolation scheme, is employed to generate the CNPS-Met
511 dataset. Unlike conventional optimal interpolation schemes that utilize a fixed influence



512 radius in the observation operator, the improved scheme adaptively adjusts the
513 influence radius based on the spatial density and distribution of observational stations,
514 thereby providing the capability to effectively characterize local variations in
515 meteorological variables.

516 The CNPS-Met dataset spans from 1980 to 2016 and covers the entire Chinese
517 mainland. It features a daily temporal resolution and a 25 km spatial resolution. The
518 dataset includes eight meteorological variables and eleven high-impact weather events,
519 categorized into generation-side, grid-side and demand-side perspectives. Evaluation
520 results indicates that, the meteorological estimates from the CNPS-Met dataset
521 generally demonstrate superior performance compared to the other three datasets
522 (CN05.1, CMFD and CDMet). This advantage is consistent across various
523 meteorological variables and throughout most regions of China, as evidenced by lower
524 *MREs* and higher *GPI* values. Furthermore, CNPS-Met maintains higher accuracy in
525 most years, seasons, and months. Compared to the other datasets, the estimated *MREs*
526 of 2-m air temperature, 2-m specific humidity, 10-m wind speed, precipitation and
527 surface pressure averaged over the Chinese mainland from 1980 to 2016 in CNPS-Met
528 could be reduced by 1.7%-18.5%, 9.0%-29.6%, 1.9%-8.5%, 2.7%-18% and 4.9%-5.2%,
529 respectively.

530 Based on the observation experiments, ideal experiments, and literature research,
531 a series of high-impact weather events critical to the operation of new-type power
532 systems are identified. In the generation-side, the frequency and mean intensity of cut-
533 out wind speed, cut-in wind speed, low radiation, extreme high temperature and



534 extreme low temperature in China are 0.4% and 37.3 m s^{-1} , 58.9% and 1.5 m s^{-1} , 14.9%
535 and 30.1 W m^{-2} , 2.5% and $37.1 \text{ }^{\circ}\text{C}$, 9.9% and $-23.1 \text{ }^{\circ}\text{C}$, respectively. In the grid-side,
536 the frequency and mean intensity of ice accretion, snowfall and conductor galloping
537 events in China are 2.36% and 0.26, 1.03% and 0.75 mm, and 12.18% and 0.25,
538 respectively. In the demand-side, the frequency and mean intensity of extreme high
539 temperature, extreme low temperature and heat and humid environment in China are
540 0.73% and 40.94°C , 24.84% and $-15.06 \text{ }^{\circ}\text{C}$, and 6.07% and 0.24, respectively.

541 Results of this study are anticipated to establish a foundation for research and
542 applications spanning meteorology and new-type power systems, and are expected to
543 ultimately support the formulation of renewable energy policies in China. Our future
544 work will focus on investigating the direct (e.g., damage to, failure of, and performance
545 degradation in power generation equipment) and indirect (e.g., reduced power
546 generation efficiency and increased operation and maintenance costs) impacts of
547 meteorological conditions on the generation-side, grid-side, and demand-side of the
548 new-type power system through field observations or idealized experiments, thereby
549 establishing a more comprehensive and scientific identification for high-impact weather
550 events, especially the compound weather events. Additionally, influences of high-
551 impact weather events on wind and solar energy are different, which will also be
552 investigated. Furthermore, we intend to update this dataset continuously and enhance
553 the spatiotemporal resolution and quality of the CNPS-Met dataset by applying artificial
554 intelligence methods (including image enhancement techniques etc.) and incorporating
555 underlying surface characteristics and satellite data.



556

557

558 **Acknowledgements**

559 This study is supported by the Research Program of Global Energy
560 Interconnection Group Co., Ltd. (SGGE0000JYJS2400043; SGGE0000JJJS2500093),
561 the National Science Foundation of China (42275004), the Key Research and
562 Development Program of Gansu Province of China (23YFFA0001), and the
563 Fundamental Research Funds for the Central Universities (lzujbky-2024-ey08).

564

565 **Data availability statement**

566 The CNPS-Met dataset is available in its most updated version from our public
567 repository at <https://www.doi.org/10.12072/ncdc.nieer.db6972.2025> (Zhang et al.
568 2025). Data are provided as standard NetCDF format. Unit conventions and detailed
569 variable descriptions are included in the metadata and the paper.

570

571 **Author contributions**

572 FZ: data curation, conceptualization, methodology, writing–original draft,
573 writing–review and editing. KB: methodology, data analysis and visualization, writing–
574 review and editing. XC: project administration, funding acquisition, writing–review
575 and editing. YY: supervision, writing–review and editing, project. FY: project
576 administration, funding acquisition. CW: supervision, conceptualization, writing–
577 review and editing.



578

579 **Competing interests**

580 The contact author has declared that none of the authors has any competing
581 interests.

582

583



584 **References**

- 585 Akmaev, R. A. 1999: A prototype upper-atmospheric data assimilation scheme based
586 on optimal interpolation: 1. Theory. *Journal of Atmospheric and Solar-Terrestrial*
587 *Physics*, 61(6), 491–504. [https://doi.org/10.1016/S1364-6826\(99\)00006-1](https://doi.org/10.1016/S1364-6826(99)00006-1).
- 588 Alonso, Y., Martinez, Y., Roque, A., et al., 2018: A post-processing module based on
589 Cressman's analysis to improve the Wind Energy Simulation Toolkit mapping
590 system. *Wind Engineering*, 43(3), 277–298. DOI:10.1177/0309524X18780400.
- 591 Baldwin, J. W., Benmarhnia, T., Ebi, K. L., et al. 2023: Humidity's role in heat-related
592 health outcomes: a heated debate. *Environmental Health Perspectives*, 131(5),
593 055001. <https://doi.org/10.1289/EHP11807>.
- 594 Bannister, R. N., 2008: A review of operational methods of variational and ensemble-
595 variational data assimilation. *Quarterly Journal of the Royal Meteorological*
596 *Society*, 134 (637), 1791-1816. <https://doi.org/10.1002/qj.2982>.
- 597 Bi, K., Chen, X., Cui, H. et al. 2025: Influence of Extreme Climate events on wind and
598 Solar Energy over the Gobi Desert Region of China in the future. *Theor Appl*
599 *Climatol* 156, 130. <https://doi.org/10.1007/s00704-025-05362-w>.
- 600 Carrassi, A., Bocquet, M., Hannart, A., et al., 2018: Data assimilation in the geosciences:
601 An overview of concepts, issues, and perspectives. *Wiley Interdisciplinary*
602 *Reviews: Climate Change*, 9(5), e535. <https://doi.org/10.1002/wcc.535>.
- 603 Chen P. Y., Y. Wang, X. S. Wen, et al., 2010: Overview of the destructive impact of low-
604 temperature rain, snow, and freezing disasters on China's power grid. *Power Grid*
605 *Technology*, 34 (10): 135-139. DOI:10.1109/CCECE.2010.5575154.



- 606 Christensen, M. F., Heaton, M. J., Rupper, S., et al. 2019: Bayesian Multi-Scale Spatio-
607 Temporal Modeling of Precipitation in the Indus Watershed. *Frontiers in Earth*
608 *Science*, 7. <https://doi.org/10.3389/feart.2019.00210>.
- 609 Cressman, G. P. 1959: An operational objective analysis system. *Monthly Weather*
610 *Review*, 87(10), 367-374. [https://doi.org/10.1175/1520-0493\(1959\)087<0367:AOOAS>2.0.CO;2](https://doi.org/10.1175/1520-0493(1959)087<0367:AOOAS>2.0.CO;2).
- 612 Daley, R. 1993: *Atmospheric data analysis* (No. 2). Cambridge university press.
613 DOI:10.4267/2042/51948.
- 614 Despotovic M, Nedic V, Despotovic D, et al., 2015: Review and statistical analysis of
615 different global solar radiation sunshine models. *Renew Sust Energ Rev* 52:1869–
616 1880. <https://doi.org/10.1016/j.rser.2015.08.035>.
- 617 D’Amico, F., Collino, E., Viterbo, et al., 2024: Fire Danger Characterization in Italy:
618 Mitigating the Impact on Real Time Operation of the Power System. 2024 AEIT
619 International Annual Conference (AEIT), 1–6. DOI:
620 10.23919/AEIT63317.2024.10736821.
- 621 Dong, D., Tao, H., Zhang, Z., et al., 2024: Projected heatwaves in Xinjiang Uygur
622 autonomous region, China. *Frontiers in Earth Science*, 12.
623 <https://doi.org/10.3389/feart.2024.1286012>.
- 624 Eyre, J. R., Bell, W., Cotton, J., et al., 2022: Assimilation of satellite data in numerical
625 weather prediction. Part II: Recent years. *Quarterly Journal of the Royal*
626 *Meteorological Society*, 148(743), 521–556. <https://doi.org/10.1002/qj.4228>.
- 627 Fu G Q., F. C. You, X. Cao, et al., 2015: Application and verification of accumulated



- 628 temperature effect in daily peak and valley load of electricity. *Journal of Applied*
629 *Meteorology*, 26 (4), 492-499. DOI: 10.11898/1001-7313.20150411.
- 630 Gandin, L.S., 1959. The problem of optimal interpolation. *Trudy Main Geophys. Obs.*
631 99, 67–75.
- 632 Gao, Y., Shao, L., Meng, Y., et al., 2025: The temporal and spatial distribution of
633 persistent low wind power events and their relationship with weather regimes in
634 mainland China. *Renewable Energy*, 252, 123523.
635 <https://doi.org/10.1016/j.renene.2025.123523>.
- 636 Giroto, M., Musselman, K. N., Essery, R. L. H. 2020: Data Assimilation Improves
637 Estimates of Climate-Sensitive Seasonal Snow. *Current Climate Change Reports*,
638 6(3), 81–94. <https://doi.org/10.1007/s40641-020-00159-7>.
- 639 Gu, X., Wang, H., Liu, H., et al., 2010: Expert System of Ice Prevention on Overhead
640 Transmission Lines. In 2010 International Conference on Intelligent Computation.
641 Technology and Automation, Vol. 2, pp. 273-276. DOI: 10.1109/ICICTA.2010.765.
- 642 Gyatso, N., Li, Y., Gao, Z., et al., 2023: Wind power performance assessment at high
643 plateau region: A case study of the wind farm field test on the Qinghai-Tibet
644 plateau. *Applied Energy*, 336, 120789.
645 <https://doi.org/10.1016/j.apenergy.2023.120789>.
- 646 He, J., Yang, K., Tang, W., et al., 2020: The first high-resolution meteorological forcing
647 dataset for land process studies over China. *Scientific Data*, 7(1), 25.
648 <https://doi.org/10.1038/s41597-020-0369-y>.
- 649 Heim, R. R., Jr. 2015: An overview of weather and climate extremes – Products and



650 trends. Weather and Climate Extremes, 10, 1–9.

651 <https://doi.org/10.1016/j.wace.2015.11.001>.

652 Hersbach H., B. Bell, P. Berrisford, et al., 2020: The ERA5 global reanalysis. Quarterly

653 Journal of the Royal Meteorological Society. 146 (730), 1999-2049.

654 <https://doi.org/10.1002/qj.3803>.

655 Hunt, B. R., Kostelich, E. J., Szunyogh, T., 2007: Efficient data assimilation for

656 spatiotemporal chaos: A local ensemble transform Kalman filter. Physica D:

657 Nonlinear Phenomena, 230(1-2), 112-126.

658 <https://doi.org/10.1016/j.physd.2006.11.008>.

659 IPCC. Climate Change 2021: the Physical Science Basis. Cambridge: Cambridge

660 University Press, 2021. Doi:10.1017/9781009157896.

661 Iver F., K. T. Thomas, 2019: A feasibility study of photovoltaic snow mitigation systems

662 for flat roofs. Technical Transactions. 12 (7), 81-96.

663 <https://doi.org/10.4467/2353737XCT.19.073.10724>.

664 Jerez S., F. Thais, I. Tobin, et al., 2015: The CLIMIX model: A tool to create and

665 evaluate spatially-resolved scenarios of photovoltaic and wind power development.

666 Renewable and Sustainable Energy Reviews, 42: 1-15.

667 <https://doi.org/10.1016/j.rser.2014.09.041>.

668 Ju G. Z., J. R. Wang, C. Cui, et al., 2022: Study on the Impact of Extreme Weather

669 Events on New Energy Power Generation and Grid Operation. Smart Power, 50

670 (11): 77-83. DOI:CNKI:SUN:XBDJ.0.2022-11-010.

671 Jiang, C., Parteli, E. J. R., et al., 2023: Evaluation of precipitation reanalysis products



- 672 for regional hydrological modelling in the Yellow River Basin. Theoretical and
673 Applied Climatology, 155(4), 2605–2626. DOI:10.1007/s00704-023-04758-w.
- 674 Jiang, Q., Li, W., Fan, Z., et al., 2021: Evaluation of the ERA5 reanalysis precipitation
675 dataset over Chinese Mainland. Journal of Hydrology, 595, 125660.
676 <https://doi.org/10.1016/j.jhydrol.2020.125660>.
- 677 Jiang, X., Xiong, X., Wang, W., et al., 2025: An Improved Interpolation Algorithm for
678 Surface Meteorological Observations via Fuzzy Adaptive Optimisation Fusion.
679 Atmosphere, 16(7), 844. <https://doi.org/10.3390/atmos16070844>.
- 680 Kalnay, E. 2003: Atmospheric modeling, data assimilation and predictability.
681 Cambridge university press. DOI:10.1017/CBO9780511802270.
- 682 Köster, R., A. Binder, 2023: Optimum 7 MW HTS direct-drive wind turbine
683 synchronous generator designs with different rotor and stator iron topologies.
684 Electrotechnics and Information Technik. 140 (2), 324-337.
685 <https://doi.org/10.1007/s00502-023-01127-3>.
- 686 Lavers, D. A., Simmons, A., Vamborg, F., et al., 2022: An evaluation of ERA5
687 precipitation for climate monitoring. Quarterly Journal of the Royal
688 Meteorological Society, 148(748), 3152–3165. <https://doi.org/10.1002/qj.4351>.
- 689 Lee, E.-H., Ha, J.-C., Lee, S.-S., et al., 2013: PM10 data assimilation over south Korea
690 to Asian dust forecasting model with the optimal interpolation method. Asia-
691 Pacific Journal of Atmospheric Sciences, 49(1), 73–85.
692 <https://doi.org/10.1007/s13143-013-0009-y>.
- 693 Lei G. L., Y. B. Shen, R. X. Huang, et al., 2025: Characteristics of small wind and low



- 694 light climate in northern Ningxia and analysis of complementary wind and solar
695 resources. *Desert and Oasis Meteorology*, 19 (3): 18-25.
696 DOI:10.12057/j.issn.1002-0799.2311.08001.
- 697 Li, J., Gao, Y., Lei, A., et al., 2025: Analysis on spatial and temporal characteristics of
698 energy supply load side affected by extreme high temperature weather in South
699 China. *Journal of Physics: Conference Series*, 2993(1), 012019.
700 DOI:10.1088/1742-6596/2993/1/012019.
- 701 Li J. H., Y. F. Cheng, J. G. Gong, et al., 2015: Improvement and Application of
702 Meteorological Geography Method in Drawing Dance Distribution Maps. *China*
703 *Electric Power*, 48 (04): 121-126. DOI:CNKI:SUN:ZGDL.0.2015-04-040.
- 704 Lin, S., Liu, C. 2012: Data assimilation of Island climate observations with large - scale
705 re - analysis data to high - resolution grids. *International Journal of Climatology*,
706 33(5), 1228 - 1236. DOI:10.1002/joc.3507.
- 707 Lindskog, M., Landelius, T. 2019: Short-Range Numerical Weather Prediction of
708 Extreme Precipitation Events Using Enhanced Surface Data Assimilation.
709 *Atmosphere*, 10(10), 587. <https://doi.org/10.3390/atmos10100587>.
- 710 Liu, Y., Yu, J., Shen, Y., et al., 2016: A Modified Interpolation Method for Surface Total
711 Nitrogen in the Bohai Sea. *Journal of Atmospheric and Oceanic Technology*, 33(7),
712 1509–1517. <https://doi.org/10.1175/JTECH-D-15-0250.1>.
- 713 Lovell-Smith, J. W., Pearson, H. 2005: On the concept of relative humidity. *Metrologia*,
714 43(1), 129–134. DOI:10.1088/0026-1394/43/1/018.
- 715 Meng, C., Xu, Y., Li, Q., et al., 2019: Analyses of observed features and future trend



716 of extreme temperature events in Inner Mongolia of China. Theoretical and
717 Applied Climatology, 139 (1-2), 577–597. [https://doi.org/10.1007/s00704-019-](https://doi.org/10.1007/s00704-019-02969-8)
718 [02969-8](https://doi.org/10.1007/s00704-019-02969-8).

719 Miatselskaya, N., Milinevsky, G., Bril, A., et al., 2022: Application of Optimal
720 Interpolation to Spatially and Temporally Sparse Observations of Aerosol Optical
721 Depth. Atmosphere, 14(1), 32. <https://doi.org/10.3390/atmos14010032>.

722 Millin, O. T., Furtado, J. C., Malloy, C. 2024: The impact of North American winter
723 weather regimes on electricity load in the central United States. npj Climate and
724 Atmospheric Science, 7(1), 254. <https://doi.org/10.1038/s41612-024-00803-1>.

725 Mohammad, A. K., A. R. Majed, C. A. Gueymard, et al., 2021: Performance analysis
726 of a 10-MW wind farm in a hot and dusty desert environment. Part 2: Combined
727 dust and high-temperature effects on the operation of wind turbines. Sustainable
728 Energy Technologies and Assessments. 47, 101461.
729 <https://doi.org/10.1016/j.seta.2021.101461>.

730 Oakland, J., Oakland, J. S. 2007: Statistical process control. Routledge.
731 <https://doi.org/10.4324/9780080551739>.

732 Oleson, K. W., Lawrence, D. M., Bonan, G. B., et al., 2013: Technical description of
733 version 4.5 of the Community Land Model (CLM). Technical description of
734 version 4.5 of the Community Land Model (CLM) (2013) NCAR/TN-503+ STR,
735 503. DOI:10.5065/D6RR1W7M.

736 Oloufemi, F., F. Zoé, I. Hussein, 2016: Ice protection systems for wind turbines in cold
737 climate: characteristics, comparisons and analysis. Renewable and Sustainable



- 738 Energy Review, 65, 662-675. <https://doi.org/10.1016/j.rser.2016.06.080>.
- 739 Pan X. M., X. F. Zhu, Z. Q. Huang, et al., 2012: The Relation Between the Strong Wind
740 Region Along One Hundred Kilometer of Railway and the Topography in Xinjiang.
741 Meteorology, 38 (2), 234-237. DOI:10.1007/s11783-011-0280-z.
- 742 Pei S. Q., M. Y. Li, Y. B. Shen, et al., 2024: Temporal and spatial pattern analysis of
743 high impact weather in wind power systems. Meteorology and Environmental
744 Science, 47 (6): 54-64. DOI:10.16765/j.cnki.1673-7148.2024.06.007.
- 745 Qin, R., Zhao, Z., Xu, J., et al., 2022: A high-resolution (1 d, 1 km) and long-term
746 (1961–2019) gridded dataset for surface temperature and precipitation across
747 China. Earth System Science Data, 14(11), 4793–4810.
748 <https://doi.org/10.5194/essd-14-4793-2022>.
- 749 Qiu, L., Shi, Z., Wu, Y., et al., 2024: Vegetation restoration enhances the regional water
750 vapor content by intensifying the inflow from the lower atmosphere on the Loess
751 Plateau in China. Climate Dynamics, 62(10), 9431–9445.
752 <https://doi.org/10.1007/s00382-024-07401-0>.
- 753 Rao, P., Wang, F., Yuan, X., et al., 2024: Evaluation and comparison of 11 sets of
754 gridded precipitation products over the Qinghai-Tibet Plateau. Atmospheric
755 Research, 302, 107315. <https://doi.org/10.1016/j.atmosres.2024.107315>.
- 756 Shaffer, B., Quintero, D., Rhodes, J. 2022: Changing sensitivity to cold weather in
757 Texas power demand. Iscience, 25(4). <https://doi.org/10.1016/j.isci.2022.104173>.
- 758 Shi, J., Wen, K., Cui, L. 2016: Temporal and spatial variations of high-impact weather
759 events in China during 1959–2014. Theoretical and Applied Climatology, 129(1-



- 760 2), 385–396. <https://doi.org/10.1007/s00704-016-1793-y>.
- 761 Shen, Q., Li, X. 2010: Method to Calculate the Critical Non-Icing Current on
762 Transmission Line Considering the Impact of Humid Air Parameters. In 2010
763 Asia-Pacific Power and Energy Engineering Conference, 1-4.
764 DOI:10.1109/APPEEC.2010.5448175.
- 765 Song W., Y. Liu, Z. Wang, et al., 2022: A novel wind turbine control strategy to
766 maximize load capacity in severe wind conditions. Energy Reports, 8: 7773-7779.
767 <https://doi.org/10.1016/j.egy.2022.06.005>.
- 768 Sullivan, P., Colman, J., Kalendra, E. 2015: Predicting the response of electricity load
769 to climate change. National Renewable Energy Lab.(NREL), Golden, CO (United
770 States). DOI: 10.2172/1215283.
- 771 Sun, R. F., H. X. Xu, L. L. Wu, et al., 2022: Statistics on low temperature weather in
772 China and its impact on wind power generation. Global Energy Internet. 5 (1), 2-
773 10. DOI:10.19705/j.cnki.issn2096-5125.2022.01.002.
- 774 Sundaram, L., Go, Y. I. 2024: Correlations of System Degradation, Losses and
775 Significant Parameters for 49 MW Large Scale Solar Plant with Real Site Data
776 Validations. Clean Energy and Sustainability, 3(1), 10022.
777 DOI:10.70322/ces.2024.10022.
- 778 Sutanto, S. J., Syaehuddin, W. A., de Graaf, I., 2024: Hydrological drought forecasts
779 using precipitation data depend on catchment properties and human activities.
780 Communications Earth & Environment, 5(1).
781 <https://doi.org/10.1038/s43247-024-01295-w>.



- 782 Talagrand, O. 1997: Assimilation of observations, an introduction (gtspecial issue\data
783 assimilation in meteorology and oceanography: Theory and practice). Journal of the
784 Meteorological Society of Japan. Ser. II, 75(1B), 191-209.
785 https://doi.org/10.2151/jmsj1965.75.1B_191.
- 786 Tsujimoto, K., Iisaka, H., Shimojima, K., et al. 1983: Report on experimental
787 observation of galloping behaviour in 8-bundled conductors. IEEE Transactions
788 on Power Apparatus and Systems, (5), 1193-1201.
789 DOI:10.1109/TPAS.1983.318060.
- 790 Ubaldi, F., Lussana, C., Salvati, M. 2008: Three-dimensional spatial interpolation of
791 surface meteorological observations from high-resolution local networks.
792 Meteorological Applications, 15(3), 331 – 345. <https://doi.org/10.1002/met.76>.
- 793 Wang, C., Zhang, W., Zou, S., et al., 2023: Spatiotemporal Heterogeneity of
794 Temperature and Precipitation in Complex Terrain along the Northeastern Margin
795 of the Tibetan Plateau. Atmosphere, 14(6), 988.
796 <https://doi.org/10.3390/atmos14060988>.
- 797 Wang, R., Fu, Y., He, Y., et al., 2022: Characteristics of extreme precipitation and
798 related near surface atmospheric conditions in summer over the Tibetan Plateau
799 from GPM observations and multi-source reanalysis datasets. Atmospheric
800 Research, 279, 106400. <https://doi.org/10.1016/j.atmosres.2022.106400>.
- 801 Wei, S., Wang, X., Wang, K., et al., 2023: Rethinking spatiotemporal variations in air
802 temperature over the Qilian Mountains, Western China, from 1979 to 2018.
803 Atmospheric Research, 286, 106671.



- 804 <https://doi.org/10.1016/j.atmosres.2023.106671>.
- 805 Wesley C., G. Daniel, H. Jonathan, et al., 2020: Considerations for maintaining resource
806 adequacy of electricity systems with high penetrations of PV and storage. Applied
807 Energy. 279, 115795. <https://doi.org/10.1016/j.apenergy.2020.115795>.
- 808 Wen, X., Zhu, X., Li, M., et al., 2023: Creation and Verification of a High-Resolution
809 Multi-Parameter Surface Meteorological Assimilation Dataset for the Tibetan
810 Plateau for 2010–2020 Available Online. Remote Sensing, 15(11), 2906.
811 <https://doi.org/10.3390/rs15112906>.
- 812 Wu J., X. J. Gao, 2013: A gridded daily observation dataset over China region and
813 comparison with the other datasets. Chinese Journal of Geophysics, 56(4): 1102-
814 1111. DOI:10.6038/cjg20130406.
- 815 Wu J., X. J. Gao, F. Giorgi, et al., 2017: Changes of effective temperature and cold/hot
816 days in late decades over China based on a high-resolution gridded observation
817 dataset. International Journal of Climatology. 37 (S1), 788–800.
818 <https://doi.org/10.1002/JOC.5038>.
- 819 Xin, B. A. 2023. New Power System and New Energy System. China Electric Power
820 Press.
- 821 Xu, Y., Zhao, P., Si, D., et al., 2019: Development and preliminary application of a
822 gridded surface air temperature homogenized dataset for China. Theoretical and
823 Applied Climatology, 139(1–2), 505–516. DOI:10.1007/s00704-019-02972-z.
- 824 Yang, L., Yuhui, W., Xiaomin, L., et al., 2015: Spatial Distribution and Temporal
825 Change in Extreme Weather Events in Three Provinces in Northeast China.



- 826 DOI:CNKI:SUN:ZRZY.0.2015-12-020.
- 827 Yang, T., Li, Q., Liu, W., et al. 2019: Spatiotemporal variability of snowfall and its
828 concentration in northern Xinjiang, Northwest China. Theoretical and Applied
829 Climatology, 139(3-4), 1247–1259. <https://doi.org/10.1007/s00704-019-02994-7>.
- 830 Yang X. Y., X. X. Huang, X. X. Gao, et al, 2022: High-temperature power reduction
831 state identification for wind turbines using feature correlation analysis and deep
832 learning methods. Forschung in Ingenieurwesen. 86 (2): 225-239.
833 <https://doi.org/10.1007/s10010-022-00586-y>.
- 834 Yao, Z., Li, X., Xiao, J. 2018: Characteristics of daily extreme wind gusts on the
835 Qinghai-Tibet Plateau, China. Journal of Arid Land, 10 (5), 673–685.
836 <https://doi.org/10.1007/s40333-018-0094-y>.
- 837 Zhao, Y., He, Z., Jiang, Y. 2024: The Inversion of Three-Dimensional Ocean
838 Temperature and Salinity Fields for the Assimilation of Satellite Observations.
839 Journal of Marine Science and Engineering, 12(4), 534.
840 <https://doi.org/10.3390/jmse12040534>.
- 841 Zhang, C., Ji, J., Wang, C., et al., 2024: Annual analysis and comparison of the
842 comprehensive performance of a CdTe PV ventilated window integrated with
843 vacuum glazing in different climate regions. Renewable Energy, 223, 120029.
844 <https://doi.org/10.1016/j.renene.2024.120029>.
- 845 Zhang, J., Liu, B., Ren, S., et al., 2024: A 4 km daily gridded meteorological dataset for
846 China from 2000 to 2020. Scientific Data, 11(1). [https://doi.org/10.1038/s41597-](https://doi.org/10.1038/s41597-024-04029-x)
847 [024-04029-x](https://doi.org/10.1038/s41597-024-04029-x).



848 Zhang, X., Song, Y., Nam, W.-H., et al., 2024: Data fusion of satellite imagery and
849 downscaling for generating highly fine-scale precipitation. Journal of Hydrology,
850 631, 130665. <https://doi.org/10.1016/j.jhydrol.2024.130665>.

851

852